# A Tour of Soft Atomic Motions: Chemical Pressure Quadrupoles Across Transition Metal-Main Group 1:2 Structure Types

Kendall R. Kamp and Daniel C. Fredrickson\*

Department of Chemistry, University of Wisconsin-Madison, 1101 University Avenue, Madison, WI, 53706, United States

**ABSTRACT:** The rational design of materials requires an understanding of the relationships between structure and properties. In some fields, advances in computational tools and modeling have mapped out many of these connections. In the realm of intermetallics, however, principles for such relationships are still needed. Recently, we illustrated how the DFT-Chemical Pressure (CP) analysis can link geometrical motifs within crystalline arrangements to the phonon band structures of intermetallics, and thus physical properties related to vibrations and atomic motion. A key indicator here are quadrupolar CP features—distributions in which positive and negative interatomic pressures are oriented perpendicularly to one another. These quadrupoles then create low energy paths of motion for the atom that can be linked to various structural phenomena, such as anisotropic vibrations and incommensurate modulations. In this Article, we survey the presence of CP quadrupoles in a collection of TE<sub>2</sub> structures (T = transition metal, E = main group element), and the roles they play in behavior observed for these compounds. We begin by developing a metric for CP quadrupolar character, which can be calculated from the output of CP analysis. After compiling these metrics for 17 TE2 structure types, we delve deeper into four systems detected as exhibiting atomic sites with quadrupolar character: (1) the Co-Sn binary system, where the quadrupoles on the Co atoms in CuAl<sub>2</sub>-type CoSn<sub>2</sub> directs the features of its superstructure in CoSn<sub>3</sub>; (2) arsenopyrite-type CoSb2, in which the highly quadrupolar CP distributions on the Sb atoms correlate with the motions followed during the phase transition to its high-temperature marcasite-type form; (3) the CrSi2 structure, in which the expansion of the lattice is predicted to open a helical path of potential soft motion analogous to that underlying the Nowotny Chimney Ladder series; and (4) the CdAs2 type, whose CP features anticipate an ability to incorporate Li atoms as guests. Together, these case studies highlight the potential for the CP quadrupoles to link local atomic arrangements with a variety of emergent properties in intermetallic phases.

#### 1. INTRODUCTION

Connecting structure to properties is one of the primary goals of materials chemistry. For intermetallic phases—solid state compounds composed of two or more metallic elements—such relationships are still needed for diverse properties such as superconductivity, and catalysis. The gap between structure and properties in intermetallics is further widened by vast range of possible elemental combinations coupled with the boundless variability of crystal structures they can adopt. Nevertheless, immense progress has been made in connecting intermetallics and their properties: the phonon-glass/electron-crystal model provides a guiding principle for the search for thermoelectric materials, specific sublattice geometries are associated with unique band structures and physical behavior, search for the magnetically active elements in triangular arrangements are associated with complex phenomena arising from frustration. 20-22

Another approach to solving this question is given by the DFT-Chemical Pressure (CP) method, which takes a structure's macroscopic pressure and resolves it in terms of interatomic interactions, giving information on the packing stresses experienced by each atom (Figure 1). Those interactions that would benefit energetically from the expansion of the structure are described as experiencing positive CP. The positive CPs are balanced by other interactions that would be stabilized by the contraction of the structure, negative CPs.

The CP method has been shown to offer a window into how the geometrical features of a structure are related to its vibrational frequencies. <sup>23-26</sup> In particular, quadrupolar CP distributions around an

atom, in which positive and negative pressures are set perpendicular to one another (analogous to the lobes of the d-orbitals) have a strong influence on the phonon band structure. Motions along the negative axis of the quadrupole (QP) serve to both shorten some contacts with negative pressures and lengthen those with positive pressures, both of which are locally favorable. These are then expected to be relatively low energy (or soft) displacements. Conversely, motions along the positive axis of the QP lead to contraction along positive CPs and the stretching of the contacts with negative CP and are then anticipated to be high energy (hard) displacements. As such CP quadrupoles are hallmarks of an anisotropic environment on at atom that gives rise to easy paths of motion.

The soft motions associated with quadrupoles have previously been linked to a variety of structural phenomena, such as intricate patterns of single atom-dumbbell substitutions (Y-Co system);  $^{27}$  superstructures and incommensurability from coordinated atomic motions along helical paths or layers (the Nowotny Chimney Ladder series and  $\text{CaPd}_{5+q/2});^{25,28}$  and disordered occupation patterns within channels (Fe<sub>2</sub>Al<sub>5</sub>). However, the full extent to which CP quadrupoles open new structural and physical effects remains an unresolved question. The prevalence of these features in intermetallic structures has yet to be systematically investigated, let alone the structural phenomena that could result from them.

In this Article, we will explore the prevalence of CP quadrupoles and the physical behavior they foretell. We begin by defining a quantitative metric for the quadrupolar character of a CP distribution, and then move to analyzing a collection of  $TE_2$  intermetallic phases, where T is a transition metal (in some cases, a lanthanide), and E is a main group metal. We will then delve further into four systems that contain sites with quadrupolar CP distributions and are known to exhibit remarkable structural phenomena, including phase transitions, potential atomic diffusion, interface insertion, and Li intercalation. Altogether, these examples illustrate how the CP quadrupoles concept can underlie structure-property relationships, and the potential of applying it to the screening of structural databases for candidate materials.

(b) Anisotropic Motion Anticipated for CP Quadrupoles

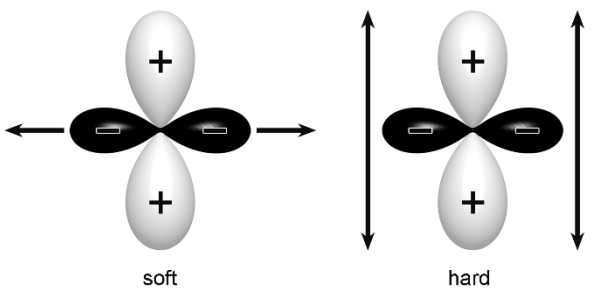


**Figure 1.** The relationship between chemical pressure quadrupoles and anisotropic atomic motion. (a) The lowest optical mode of the  $TiSi_2$  phonon band structure corresponds to motions along the negative components of the Ti and Si quadrupoles and the highest optical mode corresponds to displacements along their positive axes. (b) Soft atomic motions are anticipated along the negative directions of a quadrupole and hard atomic motions along the positive directions. Here, the CP scheme of  $TiSi_2$  is shown using the usual conventions: negative pressures are represented by black lobes and positive pressure by white lobes; the size of the lobe is proportional to the magnitude of the sum of pressure contributions in that direction.

#### 2. EXPERIMENTAL SECTION

**2.1. DFT-Chemical Pressure (CP) Analysis.** DFT-CP schemes were generated for a range of compounds sampling TE<sub>2</sub> structure types and related geometries: CdAs<sub>2</sub>, arsenopyrite-type CoSb<sub>2</sub>, marcasite-type CoSb<sub>2</sub>, rutile-type CoSb<sub>2</sub>, CrP<sub>2</sub>, CrSi<sub>2</sub>, CrSi<sub>2</sub>-type MoSi<sub>2</sub>, CrSi<sub>2</sub>-type TiSi<sub>2</sub>, CuAl<sub>2</sub>, CuAl<sub>2</sub>-type CoSn<sub>2</sub>, EuGe<sub>2</sub>-type YGe<sub>2</sub>, FeSi<sub>2</sub> (*tP*3), FeSi<sub>2</sub>-type CuGa<sub>2</sub>, fluorite-type FeSi<sub>2</sub>, NiSi<sub>2</sub>, HoSb<sub>2</sub>-type YSb<sub>2</sub>, MoSi<sub>2</sub>, MoSi<sub>2</sub>-type CrSi<sub>2</sub>, MoSi<sub>2</sub>-type TiSi<sub>2</sub>, NiAs<sub>2</sub>, PdSn<sub>3</sub>-type CoSn<sub>3</sub>, PdSn<sub>3</sub>-type CuAl<sub>3</sub>, ReB<sub>2</sub>, RuB<sub>2</sub>, ScSn<sub>2</sub>, ScSn<sub>2</sub>-type ZrSi<sub>2</sub>, TiAs<sub>2</sub>, TiSi<sub>2</sub>, TiSi<sub>2</sub>-type CrSi<sub>2</sub>, TiSi<sub>2</sub>-type MoSi<sub>2</sub>, ZnP<sub>2</sub>-type CdP<sub>2</sub>, ZrSi<sub>2</sub>, and ZrSi<sub>2</sub>-type ScSn<sub>2</sub>. Each calculation began with a

two-step geometry optimization with the ABINIT program  $^{30-33}$  using LDA-DFT $^{34}$  and Hartwigsen-Goedecker-Hutter (HGH) $^{35}$  norm conserving pseudopotentials. First, the atomic coordinates were relaxed while the unit cell vectors were held constant. In the second step, both the atomic coordinates and unit cell vectors were optimized simultaneously.

Single point calculations were then carried out on the structure's equilibrium geometry as well as slightly contracted (-0.05%, linear scale) and slightly expanded (+0.05%, linear scale) volumes to produce the local components of the Kohn-Sham potential, wavefunctions, electron densities, and kinetic energy densities. The program nonlocal, part of the CPpackage, was used to compute each atom's contribution to the nonlocal component of the potential energy. Additional computational details, including energy cutoffs and k-point meshes, are available in the Supporting Information.

The output of these programs was then used as input for the program CPpackage  $2^{36}$  to generate the CP maps. The core unwarping procedure  $^{37}$  was used in the process, along with the separation of the  $E_{\alpha}$  and  $E_{\text{Ewald}}$  terms into localized and itinerant components.  $^{36}$  The pressure maps were divided into contact volumes based on the Hirshfeld-inspired scheme,  $^{26}$  within which the pressure contributions were averaged. The resulting interatomic pressures were projected onto atom-centered spherical harmonics, and finally visualized with an in-house MATLAB program.

The assignment of the localized and itinerant electron counts on each atom for the partitioning of the  $E_{Ewald}$  and  $E_a$  terms was determined with the standard calibration procedure. See Sets of single point calculations were carried out based on extremely contracted and expanded versions of the structure (linear scales centered on 80% and 120% respectively). At each of these volumes, the number of localized electrons on each atom was tuned so that the net pressures on the atoms were equal (within 3%), while keeping the atomic site with the most negative initial CP at zero localized electrons. The number of localized electrons at each site determined for the contracted and expanded volumes were averaged to give the number of localized electrons used for CP analysis of the equilibrium structure.

Bader charges were calculated to determine the effects that assumptions about charge transfer have in the resulting CP schemes. The program *bader* was run on the electron density of the equilibrium volume (with core densities added to the valence electron density map) to determine the atomic charges. <sup>39-42</sup> Then, free-ion electron densities were generated with the Atomic Pseudopotential Engine (APE) at differing percentages of the Bader charge, <sup>43</sup> which were then used in the contact-volume construction and core unwarping procedure. The schemes shown in the main text were calculated assuming neutral atoms (0 % of the Bader charge); CP schemes determined using different percentages of the Bader charge are available in the Supporting Information.

**2.2. Electronic Structure Analysis.** Density of states (DOS) distributions were calculated on geometrically-optimized geometries for each of the structures mentioned in this Article (listed above in section 2.1) using the Vienna ab initio Simulation Package (VASP). Calculations were performed with the projector augmented wave (PAW) potentials provided with the package and the generalized gradient approximation (GGA) in high precision mode. The energy cutoffs and k-point meshes used in the calculations are listed in the Supporting Information.

2.3. Atomic Motion and Total Energy Calculations for CoSb<sub>2</sub>. The total energies were calculated with VASP<sup>44-47</sup> for a series of intermediate structures between arsenopyrite-type and marcasite-type CoSb<sub>2</sub>, and between arsenopyrite-type and a hypothetical rutile-type form of CoSb<sub>2</sub>. In the case of the arsenopyrite to marcasite transition, the Co atoms were moved incrementally (in 60 steps) from the uneven Co-Co spacing in the arsenopyrite type to the even spacing in marcasite type. The Co atoms and cell parameters were then held in place and the Sb atoms were allowed to relax. For the case of the transition from the arsenopyrite to rutile form, the arsenopyrite cell vectors were increased incrementally (in 60 steps) to reach the expanded volume of the rutile cell. All ions within the cell were released at each step. Across this series the Co-Co distances were observed to increase incrementally until an even spacing was achieved. Across these steps, the Sb-Sb

crosslinking contact increased to a length that could no longer be considered a bonding interaction.

**2.4. Phonon Band Structure Calculations.** Phonon band structures, phonon DOS distributions, and phonon modes for TiSi<sub>2</sub>, CrSi<sub>2</sub>, and CrSi<sub>2</sub>-type TiSi<sub>2</sub> were calculated using the linear response method with ABINIT. <sup>30-33,51</sup> After the self-consistent ground state electronic structure was obtained for the optimized geometry of each phase, a non-self-consistent linear response calculation was performed at q-points corresponding to the points of the k-point mesh of the original ground state calculation. These results were then analyzed with the mrgddb and anaddb ABINIT utilities to determine force constants. The resulting phonon modes, band structures, and phonon DOS distributions were visualized with an in-house MATLAB program and are provided in the Supporting Information.

**2.5. Determination of the Dependence of Quadrupole Character on Cell Volume.** CP schemes were generated for  $TiSi_2$ -type  $CrSi_2$  and  $CrSi_2$ -type  $TiSi_2$  following the procedure outlined in Section 2.1. Subsequently, the optimized geometry of the  $TiSi_2$ -type  $TSi_2$  (T = Cr) was used as a starting point for the generation of a CP scheme for  $TSi_2$  (T = Ti) without allowing the volume to relax. The inverse, creating a CP scheme for a  $CrSi_2$ -type  $TSi_2$  (T = Ti) structure with the volume-optimized for T = Cr was also completed.

#### 3. CP QUADRUPOLES AND THE TE2 STRUCTURE LIBRARY

The DFT-CP method allows for the visualization of atomic packing strains within a structure. This is done by resolving the macroscopic internal pressure of a compound onto a 3D pressure map, which is then interpreted in terms of interatomic interactions. These interatomic pressures, referred to as *chemical pressures* (CPs), either tend to pull atoms closer to each other (negative pressure) or push them away from each other (positive pressure). CPs then correspond to the local desire of a structure to either expand or contract, permitting us to assess the optimization of the interatomic distances and coordination environments of a structure, as well as identify potential paths for easy atomic motion.

An example of the CP schemes that result from this analysis is shown in Figure 1a for  $TiSi_2$ . Here, the pressures are plotted radially around each the atomic center, with the size of the lobe being proportional to the magnitude of the sum of the pressure contributions in that direction. The colors of the lobes indicate the signs of the pressure. Black is used for negative pressure, evoking the imagery of black holes at the areas of the structure where contraction is preferred. White features correspond to positive pressures; these push toward the expansion of the structure.

In this Article, we will survey the occurrence and consequences of a particular feature that can arise in these CP schemes with particular consequences for the behavior of a system, quadrupolar CP distributions. Let's begin by defining quadrupolar character. A 'perfect' quadrupole would exactly mimic a d-orbital in its angular distribution, with the nodal surfaces separating directions of positive and negative CP. In this case, angular CP distribution around an atom,

$$CP(\theta,\phi) = \sum_{l \le l_{max}} \left( \sum_{-l \le m \le l} c_{l,m} Y_{l,m}(\theta,\phi) \right) \tag{1}$$

is entirely formed from l = 2 spherical harmonics.

Based on this, a metric for quadrupolar character, QP, can be defined, with the opposing ends having QP = 0 with no l = 2 character is present and QP = 1 for d-orbital like distribution of pressures. Such conditions are met by the expression

$$QP = \frac{\left(\sum_{m} c_{l=2,m}^{2}\right)}{\sum_{l=0}^{l_{max}=6} \left(\sum_{m} c_{l,m}^{2}\right)}$$
(2)

where the sum of the square of each of the l=2 coefficients are divided by the sum of the squares of each of the other spherical harmonics up to  $l_{max}$  (generally  $l_{max}=4$  or 6). This metric can be simply calculated from the output of a CP analysis and offers the potential to discern which structures within a database of CP schemes have the most quadrupolar character. These structures, in turn, could be prioritized for the investigation of properties associated with soft atomic motions.

To narrow down the realm of intermetallics into a workable dataset to analyze the behavior of this QP metric, we consider binary prototype structures of the form TE<sub>2</sub>, where T is a transition metal, and E is a main group element (excluding oxides and halides). This collection is particularly convenient as it is well within the validity range of the 18-n rule for intermetallics, <sup>52,53</sup> enabling us to focus more on atomic packing rather than electronic effects. To build our collection of TE<sub>2</sub> prototype structures, systematic searches were performed with the Inorganic Crystal Structural Database (ICSD) <sup>54</sup> for each transition metal/main group element pair yielding 51 unique structure types (Table 1). Of these, we selected a subset for CP calculations (highlighted structures in Table 1, 17 types, 32 phases). Some structures were chosen based on the anticipated quadrupolar character derived from their coordination environments alone (see the Supporting Information for details).

Table 1. TE<sub>2</sub> Prototype Structures

1 more 10 122110000/P 0 001 motules							
Au	ıTe <sub>2</sub>	HfGa <sub>2</sub>	NdAs <sub>2</sub>	TaSe <sub>2</sub>			
β-	FeSi <sub>2</sub>	HoSb <sub>2</sub> *	NiAs <sub>2</sub> *	$TbGe_{2} \\$			
C	$dAs_2^*$	$IrS_2$	$NiGe_2$	$ThSi_2 \\$			
C	$dP_2$	IrTe <sub>2</sub>	NiSi <sub>2</sub>	TiAs <sub>2</sub>			
C	eSe <sub>2</sub>	LaAs <sub>2</sub>	$PdS_2$	$TiSi_2$			
C	eTe <sub>2</sub>	$LaS_2$	$PdSn_2$	$UGe_2$			
C	$oSb_2$	MoAs <sub>2</sub>	$ReB_2^*$	$UTe_2$			
Cı	$rP_2$	MoS <sub>2</sub>	$ReSe_2$	$WB_2$			
Cı	$Si_2$	MoSi <sub>2</sub>	ReSi <sub>2</sub>	$ZnP_2^*$			
Cı	$aAl_2$	MoTe <sub>2</sub>	RuB <sub>2</sub> *	$ZrAs_2$			
Cı	$aP_2$	NbS <sub>2</sub>	$ScSn_2$	$ZrGa_2$			
Ει	ıGe2 <sup>*</sup>	NbSb <sub>2</sub>	SmSb <sub>2</sub>	$ZrSi_2$			
Fe	eSi <sub>2</sub>	$NbTe_2$	TaS <sub>2</sub>				

Shaded in gray: DFT-CP analysis performed. \*Selected for CP analysis from screening results (see the Supporting Information).

After the structural optimizations and CP calculations were completed, we extracted QP values for each site in the structures from the CP results following Eq. 2. From these 17 structures, QP data for 44 atomic sites were obtained, as is presented as a histogram in Figure 2. The distribution is distinctly skewed to the lower side of the scale, with a majority of the sites having QP values between 0 and 0.3, a small number of atomic sites having a QP metric value above 0.5, and no atomic sites with a value above 0.7. The limited number of atomic sites with relatively high quadrupolar character (QP  $\geq$  0.4) hints that highly quadrupolar sites are not abundant CP features, at least within this sample; rather, the majority of the atomic sites have little to no quadrupolar character.

Distribution of QP Metric Values Across TE<sub>2</sub> Structures

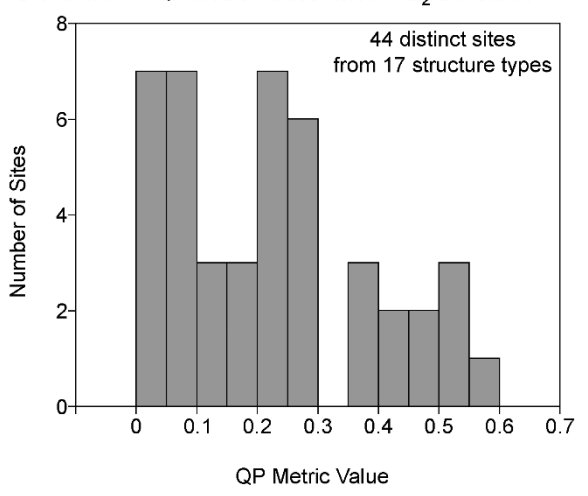


Figure 2. Histogram of QP values across TE<sub>2</sub> structure types.

In Figure 3, we highlight the ten atomic sites with the highest values for T and E atoms ordered by increasing QP value left to right. The CP functions for the highest ranked sites indeed appear like dorbitals in their distribution of positive and negative pressures, as is most obvious with the Cu atom in CuAl<sub>2</sub> with its sublime dz<sup>2</sup> orbital shape. As we move down to lower QP values, the resemblance to a d-orbital decreases, with some CP distributions now featuring more l = 1 or l = 0 character and others more complexity from l = 3 or 4 contributions.

This progression is clear on going from the very quadrupolar distribution around the Cu atoms in CuAl<sub>2</sub>, to the more dipolar distribution on the Zr atoms in ZrSi<sub>2</sub> (Figure 3). Between these two cases, the QP value decreases by almost half (from 0.4270 for Cu in CuAl<sub>2</sub> to 0.2463 for Zr in ZrSi<sub>2</sub>) and the  $l_{max}$  = 4 character even appears visually to have been approximately halved, with the Zr CP distribution having just positive and negative components separated at the equator, reminiscent of a p-orbital. The structure with the lowest QP value is the fluorite type (not shown in Figure 3), whose contributions from the l = 2 coefficients are fixed at 0 by symmetry, leading to QP = 0.

When viewing the results of Figure 3, one should keep in mind that each entry represents only one compound in the given structure type, and the same type can be adopted by compounds that are chemically quite distinct. For example, the structure type we list as  $NiSi_2$  (to make its relevance to the  $TE_2$  series clear) is formally the  $CaF_2$  (fluorite) type. As we will see in more detail below, the atomic

identity can indeed play a role in the CP value (also see the Supporting Information). The ranking should thus be regarded as providing a qualitative sense of the relative CP character of these structures. Also, the CP schemes shown here were calculated assuming the atoms are neutral for the purposes of generating the CP maps and dividing space between interatomic interactions. When charge transfer is assumed, the QP values can change as the relative magnitudes of the positive and negative pressures respond to the changing sizes of the ions. Despite this, the overall trends for quadrupole metric remain, with only some small differences arising in the site rankings (see Supporting Information).

#### 4. CP QUADRUPOLES AND ORIGIN OF THE PdSn<sub>3</sub> TYPE

**4.1. Quadrupoles in the related CuAl<sub>2</sub> and PdSn<sub>3</sub> structures in the Co-Sn system.** In our survey of QP character across TE<sub>2</sub> structure types (Figure 3), one of the most striking examples is given by the Cu atom in CuAl<sub>2</sub>. Here, the CP distribution resembles a dz<sup>2</sup> orbital with a dumbbell of negative pressure encircled with a torus of positive pressure around its equator. The CuAl<sub>2</sub> type is in fact adopted by at least 58 binary phases. S4,55 Each of these presumably exhibits similar quadrupolar CP features, which are likely suspects for any noteworthy structural phenomena in these compounds. One such example is given by the Co-Sn system, in which a CuAl<sub>2</sub>-type phase occurs alongside a related superstructure, that of CoSn<sub>3</sub>.

We begin by discussing the geometrical relationship between  $CuAl_2$ -type  $CoSn_2^{56}$  and  $CoSn_3^{.57}$  The  $CoSn_2$  structure is composed of columns of Co-centered Sn square antiprisms arranged through corner sharing in a body centered arrangement (Figure 4a). The more complex  $CoSn_3$  structure can be derived from the  $CuAl_2$  type in a simple fashion. First, we remove every third plane of Co atoms along the c direction, which creates bilayers of the  $CuAl_2$  type and layers of empty square antiprisms (Figure 4b). The overall composition is now  $CoSn_3$ . Finally, we shift every other bilayer by  $\frac{1}{2}$ 0 of the a vector of the  $CuAl_2$  type cell (Figure 4c), which converts the vacant antiprisms to distorted cubes (Figure 4d) and yields the  $CoSn_3$  structure.

Let's now consider how the CPs of the CuAl<sub>2</sub>-type  $CoSn_2$  guides this transformation. The Co atoms of the structure exhibit the expected dz<sup>2</sup>-like CP distribution (Figure 5a, inset). Large negative lobes point along the chains of Co atoms, indicating that the Co atoms are too far apart from one another. Meanwhile, the equatorial positive pressures of the quadrupoles point along heteroatomic Co-Sn contacts, suggesting the desire for the  $Co@Sn_8$  polyhedra to expand. In addition to their positive Co-Sn CPs, the Sn atoms

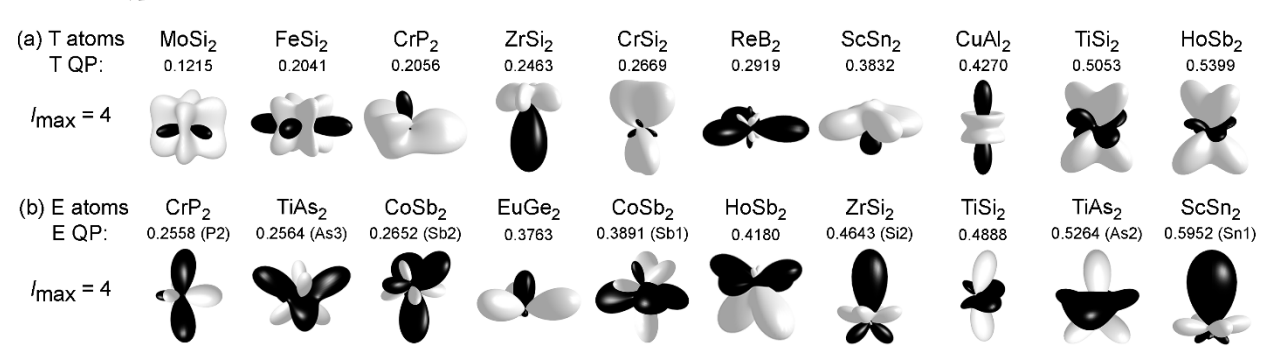
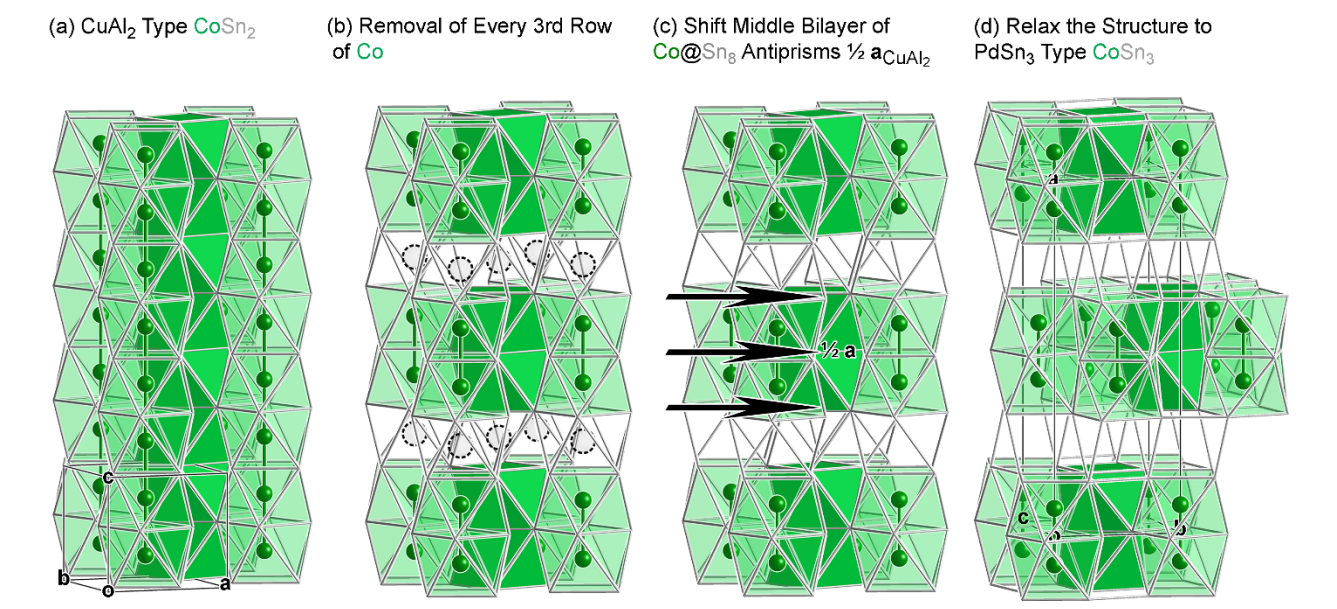


Figure 3. Highest ranked CP quadrupoles encountered in  $TE_2$  structures. CP distributions are plotted for 10 atomic sites for (a) T and (b) E atoms with  $l_{max} = 4$  distributions.



**Figure 4.** Stepwise derivation of PdSn<sub>3</sub>-type CoSn<sub>3</sub> from CuAl<sub>2</sub>-type CoSn<sub>2</sub>. (a) Beginning with the CuAl<sub>2</sub> type, (b) we remove every third layer of Co atoms along c, (c) and shift every other remaining CuAl<sub>2</sub>-type slab by  $\frac{1}{2}$  **a**, resulting in (d) in the PdSn<sub>3</sub> type.

experience positive Sn-Sn CPs directed between the columns of antiprism, expressing the need for separation of these columns. Further, the Sn-Sn contacts comprising the antiprismatic lattice are overly extended, as evident from the negative pressure along these contacts (Figure 5a). The major conflicting tensions in the structure are then the opposing needs of the Co-Co and Sn-Sn contacts withing the square antiprism columns to contract and the Co-Sn contacts to expand the antiprism in conjunction with the desire to increase intercolumn Sn-Sn distances.

Among these CP features, the quadrupolar distributions on the Co atoms are most suggestive of easy atomic motion. In particular, the large negative lobes pointing up and down along c point to displacements upwards or downwards as ways that some of the Co-Co distances could be shortened to relieve their negative CPs. However, the symmetry of the CuAl<sub>2</sub> type means that a motion toward one Co neighbor means moving away from the Co atom on the other side. As a result, the Co atoms remain at the centers of the Sn antiprisms with negative CPs symmetrically directed along  $\pm z$ . In the CoSn<sub>3</sub> structure, this challenge is solved by removing every third Co atom in the chains. Each of the remaining Co atoms then only has one Co neighbor along c, which it can move toward without straining other Co-Co contacts.

#### 4.2 Chemical Pressure relief upon superstructure formation.

We can now compare these considerations with the CP scheme of the superstructure (Figure 5b). The overall scheme bears some clear parallels with that of its parent structure. The Co-Co contacts are still marked by negative CP, while the Co-Sn CPs are still positive. However, now that the Co atoms form dumbbells rather than chains, the CPs distributions are missing one of their two large negative lobes. The Co CPs now seems to show only half of a dz2-like arrangement (Figure 5, inset). Likewise, the Sn atoms have retained many of the features of the parent structure, with negative pressures within the antiprismatic motifs and positive pressures between them. There is the added feature of positive Sn-Sn pressures along the Sn contacts bridging the antiprismatic bilayers to form the distorted primitive cubic slab (Figure 5b).

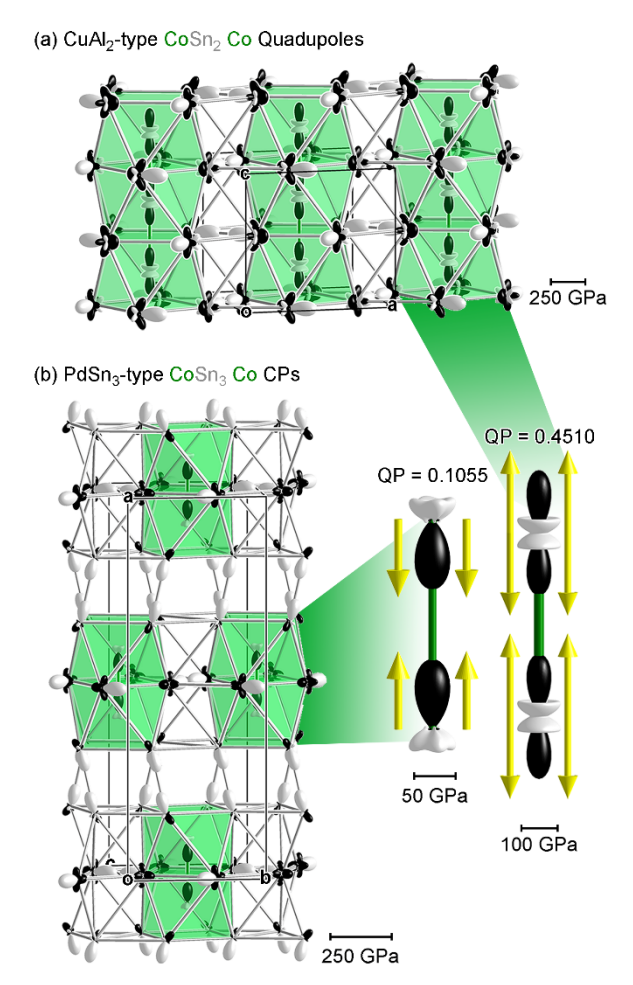


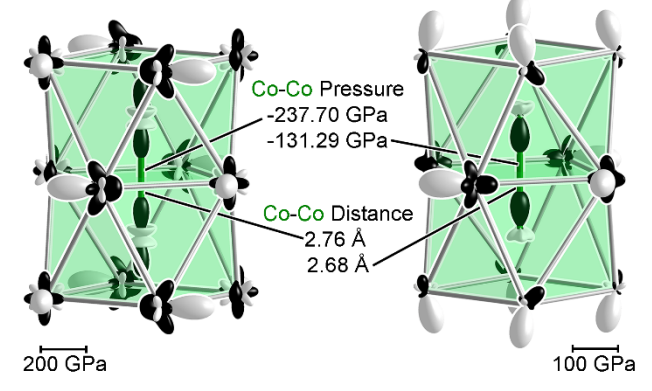
**Figure 5.** Chemical pressure schemes of PdSn<sub>3</sub>-type CoSn<sub>3</sub> and its parent structure, CuAl<sub>2</sub>-type CoSn<sub>2</sub>. (a) CuAl<sub>2</sub>-type CoSn<sub>2</sub> contains highly quadrupolar Co atoms (inset), while (b) PdSn<sub>3</sub>-type CoSn<sub>3</sub> has lost much of the quadrupolar character on its Co atoms with the Co chains becoming dumbbells.

The movement of the Co atoms towards dimer formation in  $CoSn_3$  benefits the superstructure in several ways (Figure 5, insets). The relatively high QP value of 0.45 for Co in  $CoSn_2$  hints at the structure's impetus to undergo a transition. Following the formation of the superstructure, the QP value of the Co atoms is drastically reduced to 0.11. This stark decrease in QP character indicates the Co atoms have obtained a more isotropic coordination environment.

Relief can also be seen in changes to the magnitudes of the CP features, and the atomic packing stresses they represent, as is highlighted in Figure 6 with close-up views of the Co environments. In CoSn<sub>2</sub>, the Co-Co distances along the chain are 2.76 Å, leading to a Co-Co CPs of -237.70 GPa—a strong driving force for contraction. In the PdSn<sub>3</sub> superstructure, the Co-Co distances are reduced to 2.68 Å, much closer to the sum of the metallic radii at 2.50 Å. The Co-Co CP is then nearly halved to -131.29 GPa.

 $\begin{array}{lll} \text{CP Relief in the CuAl}_2 \text{ Type to PdSn}_3 \text{ Type Transformation} \\ \text{CuAl}_2\text{-type CoSn}_2 & \text{PdSn}_3\text{-type CoSn}_3 \end{array}$ 

(a) Chemical Pressure Relief within Co-Co Contacts



(b) Chemical Pressure Relief within Positive Pressure Networks

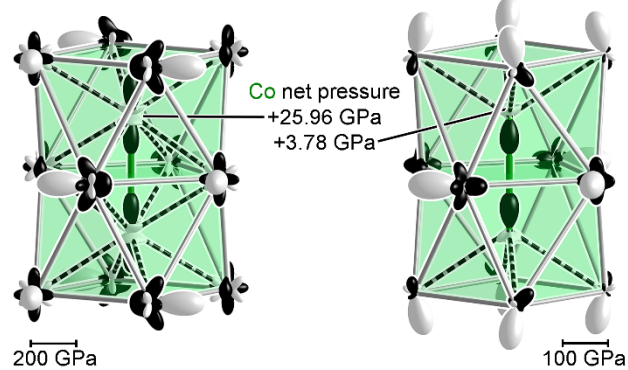


**Figure 6.** Relief of atomic packing strains upon superstructure formation in the Co-Sn system. Formation of Co-Co dumbbells relieves (a) negative CP along the shortest Co-Co contacts as well as (b) Co-Sn positive CPs. Note the different CP scalebars used in the plots for the  $CoSn_2$  and  $CoSn_3$  structures.

This effect results in lower CP magnitudes in the Co-Sn contacts. In the CuAl $_2$  type, each Co atom participates in 8 Co-Sn contacts, each of which experiences positive CP (Figure 10b, black and white dashed lines). This high number of positive CPs results in the Co atomic site having a positive net CP of +25.96 GPa, despite the presence of the large Co-Co negative pressures. Upon forming the superstructure, the number of Co-Sn contacts with positive CP is reduced to 4 (Figure 6b, right, black and white dashed lines). The net atomic CP on the Co site is then reduced to +3.78 GPa. Altogether, this

comparison highlights how the quadrupolar features of  $CoSn_2$ 's CP scheme anticipates the path the CP relief offered by the  $CoSn_3$  superstructure.

#### 5. QPs AS GUIDES TO POLYMORPHISM IN CoSb<sub>2</sub>

**5.1. Polymorphism in CoSb<sub>2</sub> and the related rutile type.** The compound  $CoSb_2$  in its arsenopyrite-type form<sup>59,60</sup> is also highly ranked in our library of CP quadrupole results, with its two symmetry-distinct Sb sites both appearing in the list of top-ten E positions. This structure corresponds to the room temperature polymorph of  $CoSb_2$ , which undergoes a transition to the marcasite-type  $CoSb_2$  at  $377\,^{\circ}C.^{61,62}$  Let's consider the role played by the QPs of the arsenopyrite form in this phase transition.

The two structures share the same basic building unit: an edgesharing column of T@E6 octahedra. These units link to each other through corner-sharing, and additional crosslinks are made between the octahedral columns by Sb-Sb bonds (Figure 7a, top). The major distinction between the structures is in the spacing of the Co atoms along the columns. In the arsenopyrite form, the Co-Co spacing exhibits a short-long pattern with distances of 3.04 and 3.70 Å, with the overall structure having monoclinic symmetry. In the marcasite type (Figure 7b, top), the Co atoms are evenly spaced at an intermediate distance of 3.40 Å, and the structure has orthorhombic symmetry. Both types are simply related to the rutile structure type: rutile contains analogous chains of TE6 octahedra but rotated relative to each other in a way that breaks the E-E crosslinks (Figure 7c, top).<sup>63</sup> The T atoms are equally spaced along these chains in the rutile type (with the distance being 3.80 Å for a DFT structural optimization of a hypothetical rutile-type CoSb<sub>2</sub> phase).

CoSb<sub>2</sub> and Related Structures with Density of States Distibutions

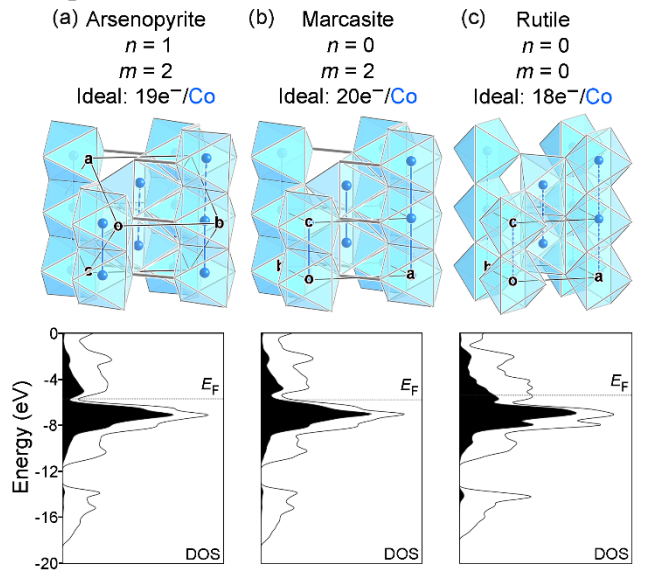


**Figure 7.** Structures, 18-n+m electron count assignments, and density of states (DOS) distributions for CoSb<sub>2</sub> in a series of structures, both experimentally observed and hypothetical: (a) the arsenopyrite type with its short-long alternation of Co-Co contacts, (b) the marcasite type, with its even spacing of Co-Co atoms, and (c) the rutile type with no electron pairs shared in Co-Co or Sb-Sb interactions (n = 0, m = 0). Contributions from Co d character to the DOS distributions are shaded.

These differing arrangements of the same repeat units have electronic consequences that can be explained with the 18-n rule.<sup>52</sup> In the 18-n bonding scheme, a T atom in a T-E intermetallic

compound is predicted to require 18-n electrons to achieve a closed shell electron configuration, where n is the number of electron pairs it shares with neighboring T atoms in *isolobal bonds*, bonding functions that involve substantial bridging contributions from E atoms, but are isolobal to direct T-T bonds. In addition, some electrons not involving the transition metal atoms may also be needed to populate E-E bonding states, which can be written as m electrons/T atom. A structure is electron-precise if its stoichiometry provides 18-n+m electrons per transition metal atom. <sup>52</sup> This scenario is then often reflected in the structure's density of states (DOS) distributions, with the Fermi Energy ( $E_F$ ) lying in or near a pseudogap.

Applying this rule to the polymorphs of CoSb<sub>2</sub>, we begin with the number of electrons given by the stoichiometry:  $9 + 2 \times 5 = 19$  electrons/Co atom, which we expect will be differently distributed among the atoms for the three structure types. First, inspection of the arsenopyrite type form suggests that it contains 1 Co-Co isolobal bond per Co atom from its short Co-Co contact in its short-long pattern of the chains, giving n = 1. In addition, each Sb atom has one Sb-Sb bond, in which 1 electron/Sb is present independent of the Co atoms. As there are two Sb atoms per Co, this gives m = 2. For this structure, an electronic pseudogap or bandgap is then expected for 18-n+m=18-1+2=19 electrons/Co atom, the number of electrons available from the stoichiometry. Indeed, the  $E_F$  lies within a pseudogap in the DOS distribution calculated for this structure (Figure 7a, bottom).

The marcasite-type CoSb<sub>2</sub> maintains the Sb-Sb crosslinks of the arsenopyrite type (m=2) but its uniform Co-Co distances are significantly longer than the short ones in the arsenopyrite-type form, suggesting that now n=0. With this n, m configuration, 18-0+2=20 electrons/Co atom would be required for a closed shell configuration, which is one higher than the 19 electrons/Co available from the stoichiometry. This deficiency is reflected in the DOS distribution, with the  $E_{\rm F}$  lying slightly below a pseudogap (Figure 7b, bottom).

The rutile type, like the marcasite type, does not contain any Co-Co bonding contacts (n = 0). However, it also does not contain any Sb-Sb crosslinks, giving m = 0. This configuration requires 18 - 0 + 0 = 18 electrons/Co, less than what is available from the stoichiometry. The electron rich nature of this type can also be detected in the DOS distribution, as the  $E_F$  lies above a shallow pseudogap (Figure 7c, bottom).

With the same repeat units but multiple electronic configurations available, one would infer that the compound would prefer the electronically precise configuration, the arsenopyrite type. This indeed is the case at room temperature, but under heating a phase transition occurs with the two potential polymorphs available through small displacements, we can then ask: why is the transition to the marcasite type preferred over that to the rutile type? As we will see next, the answer is connected to CP scheme of arsenopyrite-type CoSb<sub>2</sub>.

**5.2. Paths of motions in arsenopyrite-type CoSb**<sub>2</sub>. To begin our investigation into the role of CP quadrupoles in the polymorphism of  $CoSb_2$ , we present the CP scheme of arsenopyrite  $CoSb_2$  in Figure 8. The Co atoms appear here with white oblong surfaces indicating that the Co atom is too large for its current coordination, experiencing positive CP from the Sb atoms on all sides. Expansion at these overly short Co-Sb contacts is resisted by the negative CPs that dominate Sb-Sb interactions, particularly along the c axis. The

negative Sb-Sb pressures lie approximately perpendicular to the positive Sb-Co pressures, yielding quadrupolar character at these sites.

In the insets of Figure 8, we examine these quadrupolar features for the two symmetry-distinct Sb sites more closely. To highlight their QP character, the CP distributions here are drawn using a lower number of spherical harmonics ( $l_{max} = 2$ ). While both sites do exhibit visibly quadrupolar character in these plots, this is stronger on the Sb1 site than the Sb2 site, with QP values being 0.3891 and 0.2652 respectively (Figure 3). The difference in magnitude of these QP values comes from the Co-Co contacts that the respective Sb sites bridge: the Sb1 sites bridge the shorter Co-Co bonding contact while the Sb2 atoms bridge the longer, non-bonding Co-Co contact. The bond formed between Co atoms requires more space than a non-bonding contact would, pushing the Sb1 atoms away from it against negative Sb-Sb CPs. As the positive CPs on the Sb1 lie approximately perpendicular to the negative pressures between Sb atoms along the octahedral edges parallel to the Co chains, the quadrupolar character of the site is enhanced.

The situation is different for the Sb2 atoms, which bridge the long, non-bonding Co-Co contacts (dashed lines, Figure 8). These do not feel as strong of a repulsion as the pattern of Co dimers has the Co atoms displaced away from them. They thus experience relatively minor Co-Sb positive CPs. This positive pressure is still roughly perpendicular to the negative Sb-Sb pressures along c, giving the site some quadrupolar character, but it is lower than that of the Sb1 site.

#### Chemical Pressure Scheme of Arsenopyrite CoSb<sub>2</sub>

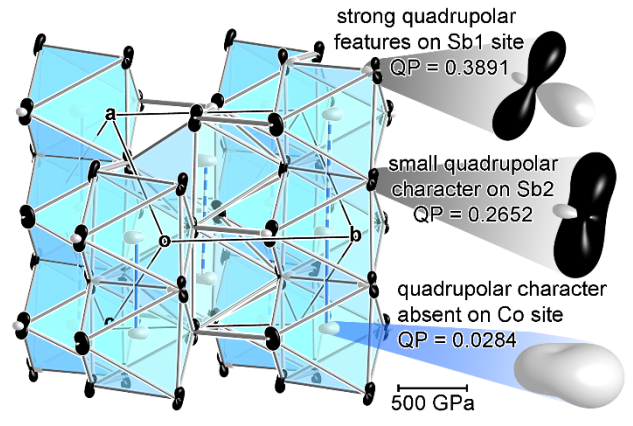


**Figure 8.** Chemical Pressure scheme of arsenopyrite-type CoSb<sub>2</sub> ( $l_{max} = 2$ ), highlighting the quadrupolar character on the Sb sites.

Based on our earlier discussion, these CP quadrupoles are expected to influence the ease with which the Sb atoms move in different directions during a phase transition to the high-temperature form of CoSb<sub>2</sub>. Displacements along the directions of the negative CP for these atoms is expected to be a relatively soft motion, and correlate with low vibrational frequencies in the phonon band structures. Conversely, displacement along the positive features of the CP quadrupoles is likely a hard motion—or high energy path—and contribute to higher frequency phonon modes. The alignment of the motions leading to the marcasite or rutile types with these CP features could then affect their relative favorability.

Let's first look at the arsenopyrite to marcasite transition (Figure 9a). To track the motions of the Sb atoms during this transition, we performed a calculation in which the Co atoms in the arsenopyrite

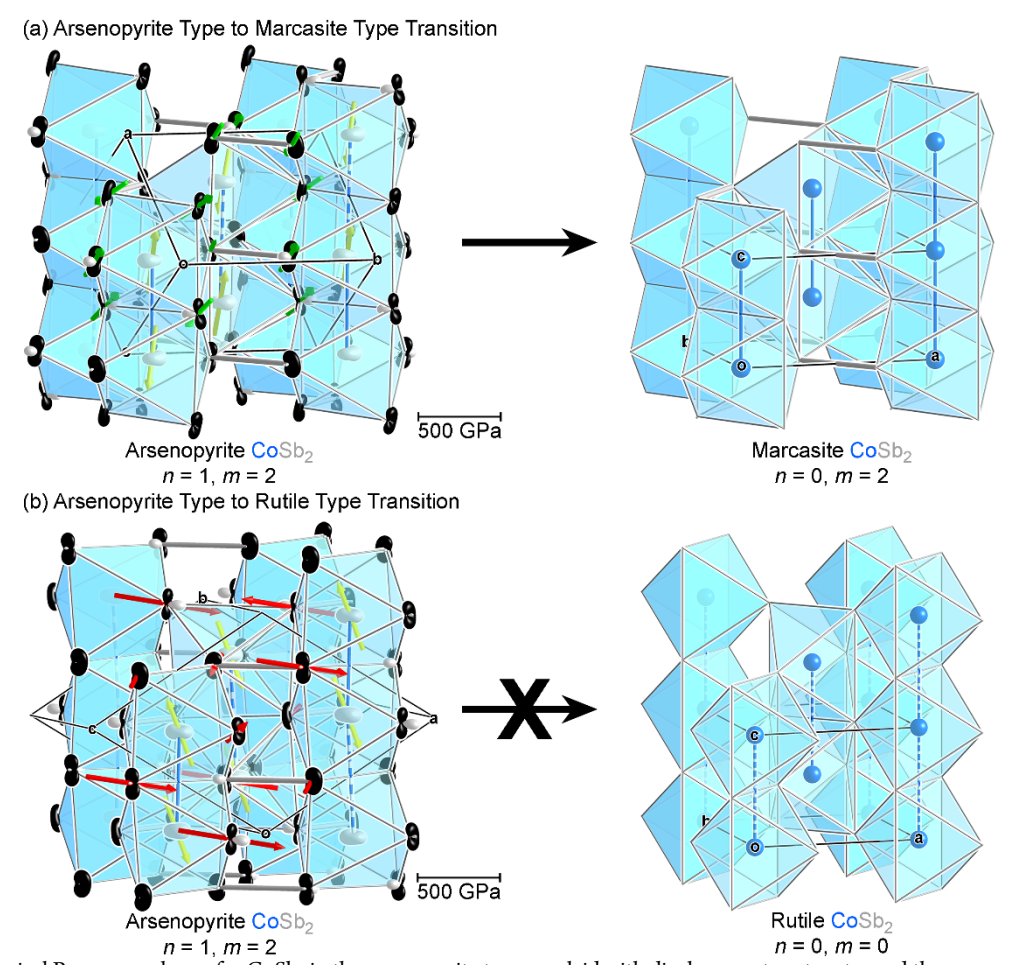


**Figure 9.** Chemical Pressures scheme for CoSb<sub>2</sub> in the arsenopyrite type overlaid with displacement vectors toward the marcasite and rutile structure types. As the Co atoms move (yellow arrows) to break their dimer pattern, positive pressures along the Co-Sb contacts force Sb displacements. (a) In the arsenopyrite to marcasite transition, quadrupolar features allow the Sb (green arrows) to move in a concerted fashion that maintains the Sb-Sb crosslinks. (b) In the arsenopyrite to rutile transition, the added dissociation of the Sb<sub>2</sub> dimers leads to Sb-Co collisions at points of positive CP.

type were moved in a stepwise fashion toward the even Co-Co spacing seen in the marcasite type. At each point, the Co atoms were then held in place and the Sb atoms were allowed to relax around them within a fixed unit cell. The initial positions of the Sb atoms are depicted on the left side of Figure 9a, with green arrows pointing along the displacements of the Sb atoms, and yellow arrows along the displacements of the Co atoms; the magnitude of the displacement is proportional to the size of the arrow.

The transition from the arsenopyrite type to the marcasite type is driven by the movement of Co atoms. Each Co atom moves away from its shorter Co contact, which simultaneously decreases the distance to its more distal Co neighbor along the Co chain. The Co atoms also displace at a slight angle off of  $\mathbf{c}$ , a result of the Co-Co chains in the arsenopyrite type not being perfectly linear.

Following the arrows of the Co atoms and their Sb neighbors shows that the movements of the two atom types are coordinated to avoid exacerbating the positive Co-Sb CPs. In terms of Sb<sub>2</sub> dimers, the displacement vectors for the two atoms are nearly parallel and pointing the same direction. They move as units, without significantly perturbing the Sb-Sb bond length. This ability of the Sb<sub>2</sub> pairs to maintain unity, while still accommodating the needs of the Co-Sb positive CPs, may be associated with the quadrupolar nature of the

Sb atoms and the flexibility it provides in how the Sb atoms respond to the Co atoms' shifting.

This is in contrast with another potential transition, that of the arsenopyrite type to a hypothetical rutile type form. This transition is explored in Figure 9b, where the motions of the atoms were calculated from a series of stepwise calculations in which the arsenopyrite cell was expanded to the cell parameters of the rutile cell with all ions relaxing, yielding an arrangement with essentially equally spaced Co atoms, and largely dissociated  $Sb_2$  dimers (though the tetragonal symmetry of the rutile type was not achieved; see below). The lefthand side of Figure 6b shows the starting positions of the Sb atoms in the arsenopyrite cells overlaid with displacement vectors for the Sb atoms and Co atoms in red and yellow, respectively (plotted using fractional coordinates to reconcile the differing cell parameters of the start and end point).

The Co-Sb positive CPs again induce the Sb atoms to move in response to the Co atoms. However, in this hypothetical transition, the  $Sb_2$  dimers also dissociate, which puts additional constraints on the Sb positions. The  $Sb_2$  separation pushes the Sb atoms into their respective octahedral chains, a movement that is along a path of positive pressure. This is not a problem for Sb atoms that bridge Co-Co contacts that are expanding. For the Sb atoms that bridge contracting Co-Co pairs, however, a collision is set up. These Sb atoms

appear in Figure 9b with very short arrows; they are trapped by the competing demands of the Co-Sb positive CP and Sb-Sb elongation.

In summary, the two transitions center on Co motion, but the Sb atoms respond to this motion very differently: in the transition to the marcasite type, concerted motions of Co atoms and Sb crosslinking pairs are possible due to the flexibility provided by the Sb QPs, while in the transition to the rutile type, such a concerted motion of Co and Sb atoms are impeded by the added requirement of the Sb2 dissociation. With the transition to the marcasite type involving concerted movements that avoid worsening the Co-Sb positive CPs and take advantage of the Sb quadrupoles, one might anticipate that the transition of the marcasite type has a lower energy cost than that to the rutile type.

# **5.3. Energetics of atomic motion in the CoSb\_2 structural transition.** To test these expectations, we performed a series of calculations on intermediate points between the arsenopyrite structure, with its uneven spacing of Co atoms, and the marcasite structure, in which the Co atoms are uniformly spaced. For each calculation, the spacing between the Co atoms was adjusted and fixed, while the positions of the Sb atoms were allowed to relax around them. The energies of the configurations across this transition are plotted in Figure 10 as the dark blue line.

This curve rises in a nearly linear shape upon moving towards the marcasite geometry, reaching its maximum value of +0.03~eV/FU (relative to the starting point) at the end of the transition. This number compares well with the relative energy of the marcasite type optimized on its own (open, dark blue circle in Figure 10). No other energy maximum is encountered, suggesting that there are no kinetic effects associated with the transition beyond the energy difference between the start and end points.

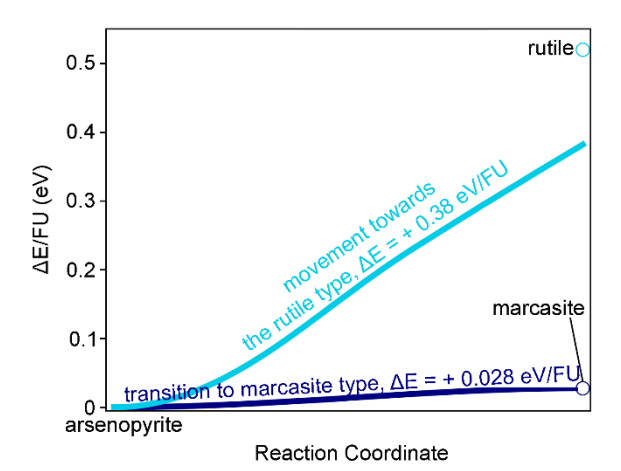


**Figure 10.** Energy vs. transition progress diagram for transitions for arsenopyrite type CoSb<sub>2</sub> toward the high-temperature marcasite form or a hypothetical rutile form. Open circles represent the marcasite and rutile types computed independently of the stepwise calculations.

A comparison with analogous calculations on the transition to the rutile type is informative. The intermediate steps along this transformation were obtained by incrementally adjusting the unit cell parameters to match those for the rutile type and relaxing the atomic positions within the fixed cells. When the rutile-type cell was obtained, the Co atoms along the chains were evenly spaced to within 0.01 Å. The Sb<sub>2</sub> dimers also showed significant lengthening (2.91 vs. 3.12 Å), but not to the extent that the Sb coordination by Co

becomes the trigonal planar; some pyramidal character remains which leads to symmetry-breaking relative to the space group of rutile. We thus refer to this endpoint as the 'pseudo-rutile' structure.

The energy change across this transformation is plotted in Figure 10 as a light blue line. The curve the climbs upwards but with a much steeper slope than for the arsenopyrite to marcasite transition. It reaches +0.38 eV/FU relative to the arsenopyrite starting point, without crossing a transition state. The resistance to forming the true rutile structure is understandable from the viewpoint of energetics (it is +0.52 eV/FU higher in energy than the arsenopyrite structure; see light blue circle in Figure 10), as well as the observation that this geometry would shorten Co-Sb contacts that already experience positive CP in the arsenopyrite type.

When comparing these curves, it is clear that the energetics for the two transitions are quite different. The cost of transforming to the rutile type is 10 times higher/FU than going to the marcasite type. This aligns with the experimental observations: the marcasite structure type appears as a high-temperature polymorph of CoSb<sub>2</sub>, with no indications that a rutile form exists.

## 6. CHIMNEYS, LADDERS, AND STRUCTURAL SERIES BASED ON THE CrSi<sub>2</sub> AND TiSi<sub>2</sub> STRUCTURES

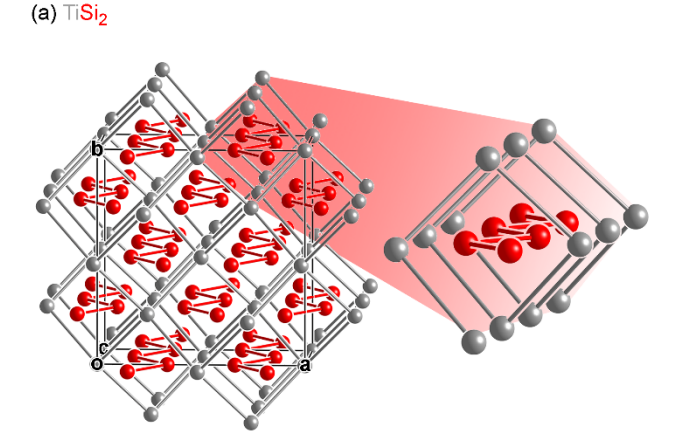
Our survey of  $TE_2$  compounds also uncovered highly quadrupolar CP distributions for the  $TiSi_2$  and  $CrSi_2$  structures ( $TiSi_2$  and  $CrSi_2$  are  $2^{nd}$  and  $6^{th}$  in the T atom distributions, respectively, and  $TiSi_2$  also comes up as  $3^{rd}$  for E sites). As has been described previously (and illustrated in the Supporting Information), the relationship between these structures is clearly seen by considering them in terms of stacks of Si honeycomb nets whose hexagons are occupied by T atoms.  $^{64-66}$  The stacking of these layers, in which the T atoms of one layer lie above Si-Si edges in the layers above and below, differentiates the two structure types (as well as the  $MoSi_2$  type): in the  $TiSi_2$  type, the  $T@Si_6$  honeycomb layers are offset from one another in an ABCD sequence, while in the  $CrSi_2$  type they adopt an ABC stacking.

In the  $TiSi_2$  type, the stacking of the  $T@Si_6$  honeycomb layers creates a flattened diamond network of Ti atoms (Figure 11a), forming square channels built from 4-fold helices al running along the c-direction. These channels are then stuffed with Si zigzag chains (Figure 11a).  $^{67,68}$  The same helical channels can also be found in the  $CrSi_2$  type, but in a bit more complicated fashion. Due to the ABC stacking of the  $Cr@Si_6$  honeycomb nets, they now travel in several different directions. In the hexagonal setting of the  $CrSi_2$  cell, the helices run in ab plane with orientations that depend on their heights along c. As one moves along c, the helices become rotated by 60° relative to those above and below. Some helices run along the a axis, others along b axis, and still others along a+b (Figure 11b).  $^{69,70}$ 

Despite the different arrangements of the helical motifs in the two structure types, the coordination environments of the T atoms and the Si atoms remain very similar. In each, the T atoms are coordinated by 4 T neighbors forming elongated and twisted tetrahedra as well as an analogous tetrahedra of the closest Si neighbors (in neighboring honeycomb layers); a belt of 6 Si atoms in a ring then runs around the equators of these arrangements. This coordination gives both the Cr and Ti atoms in their respective structure types similar CP distributions: each T atom experiences positive pressures from the nearest Si atoms, with negative pressures towards the Si atoms in the same honeycomb sheet taking up much of the remaining angular ranges—quadrupolar arrangements result (Figure 12). It should be

noted, though, that the negative CPs along the longer Cr-Si contacts are of a much smaller in magnitude than their Ti-Si analogs in TiSi<sub>2</sub>. This decreased magnitude hints at greater constraints in the potential atomic motions in the CrSi<sub>2</sub> structure.

Helical Motifs in TiSi2 and CrSi2



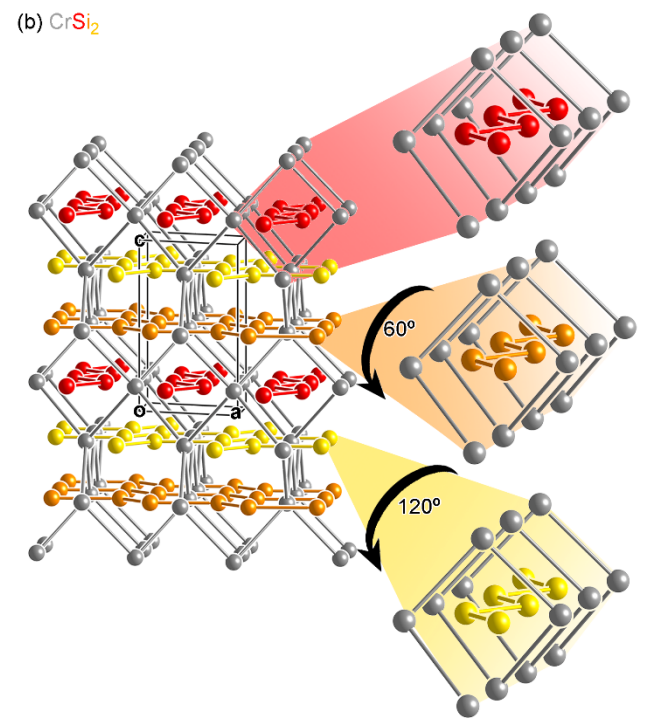


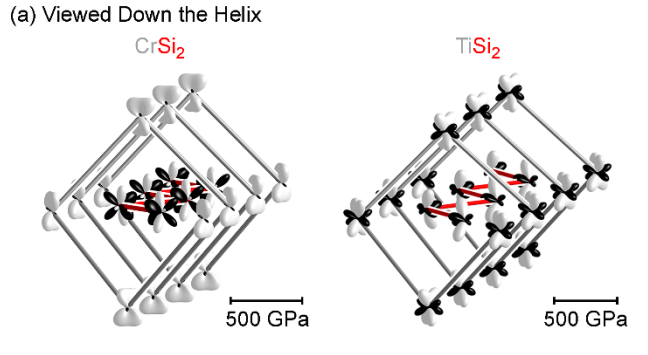
**Figure 11.** Arrangements of helical motifs in the  $TiSi_2$  and  $CrSi_2$  types. (a) Parallel T atom channels in  $TiSi_2$ . (b) T atom channels related by  $6_4$  screw operations in  $CrSi_2$ .

In  $TiSi_2$ , the Si atoms also display significant quadrupolar character. The distribution of the CPs can be loosely compared to that of a  $dz^2$  orbital: with positive pressure running along one axis and negative lobes at its equator. Here, positive CPs along the shortest Ti-Si contacts are again in competition with negative CPs, this time along the Si-Si and remaining Ti-Si interactions (Figure 12). The cumulative effect of these pressures is a distribution with strong positive CP lobes along nearly opposite directions, with negative pressure occupying the remainder of the angular space.

Some of these features are also recognizable in the CP distributions for the Si atoms of the CrSi<sub>2</sub> type. However, the reduction in the Cr-Si negative pressures leads to a spikier arrangement of the CP

lobes, with some positive CPs emerging in between. This reduces the d-orbital-like appearance of the function. Indeed, upon going from  $TiSi_2$  to  $CrSi_2$ , the CP quadrupole metric value for the Si atoms drop significantly from 0.49 to 0.23.

#### Chemical Pressure in Helical Motifs



(b) Viewed Perpendicular to Helix

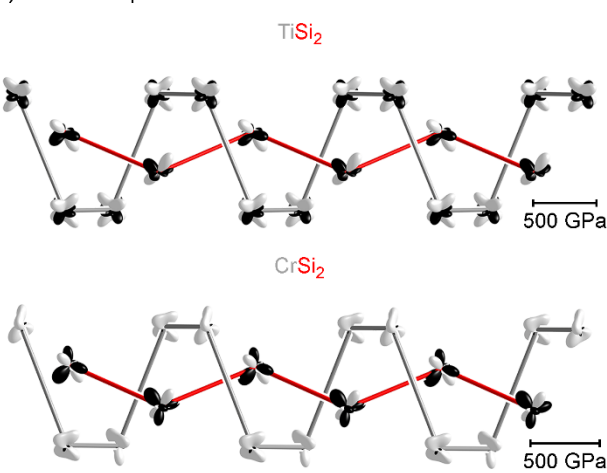


**Figure 12.** Chemical Pressure schemes of TiSi<sub>2</sub> and CrSi<sub>2</sub>. (a) Views down the helical channels. (b) Side views of the helices. Note that the negative pressures on the Si atoms in TiSi<sub>2</sub> are more in-line quadrupolar character than their analogs in CrSi<sub>2</sub>.

This difference can be correlated to a stark contrast in the structural chemistries offered by these structure types. For the TiSi<sub>2</sub> type, the quadrupoles on the E sites along each channel align to create a helical path of easy motion for the E atoms.<sup>28</sup> This flexibility is demonstrated by the Nowotny Chimney Ladder (NCL) series (Figure 13).<sup>28</sup> Here, the T atoms maintain the flattened diamond network forming the square chimney lattices in the TiSi<sub>2</sub> type, while the E atoms form another set of helices in place of the original zigzag chains.<sup>67,71-73</sup> The positions of these E atoms adhere closely to the helical path traced out by the CP quadrupoles of the TiSi<sub>2</sub> type, testifying to how changes in the T:E ratio are easily accommodated by small shifts along this path.

However, no such superstructure chemistry has been reported for the  $CrSi_2$  type despite the fact that it contains analogous T atom channels. This observation can be attributed to the smaller QP value calculated for the Si atoms in  $CrSi_2$ . Where does this difference in quadrupolar character come from—the change in structure type or the switch from Ti to Cr? Clues to the answer of this question can be found in CP schemes calculated for hypothetical  $TiSi_2$  and  $CrSi_2$  compounds with their structure types reversed (Table 2). The Si

QP value calculated for  $CrSi_2$ -type  $TiSi_2$  is 0.46, much closer to that of the original  $TiSi_2$  structure (0.49) than that for  $CrSi_2$  in its own type (0.23). Likewise,  $TiSi_2$ -type  $CrSi_2$  has a Si CP-QP value of 0.29 which is only moderately increased from that obtained for its own structure (again, 0.23) and far below that for  $TiSi_2$  (0.49). Together, these observations suggest that the identity of the T element has a larger impact on the QP values than the structure type itself.

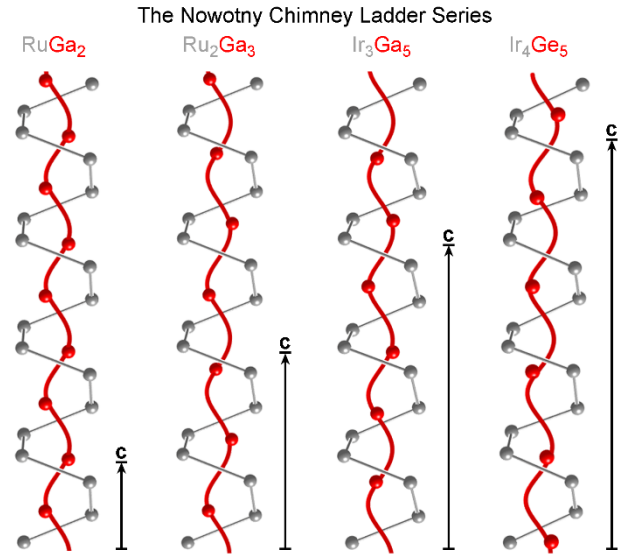


**Figure 13.** The Nowotny Chimney Ladder series arising from the soft atomic motions of main group atoms along helical paths present in the parent  $TiSi_2$  type.

Table 2. QP Metric Values for TSi<sub>2</sub> Compounds at Different Volumes and Structure Types.

· 01411100 4114 0014101410 1/P 001							
Phase	Type	Volume	T QP	Si QP			
TiSi <sub>2</sub>	TiSi <sub>2</sub>	T = Ti	0.5053	0.4888			
$CrSi_2$	$CrSi_2$	T = Cr	0.2669	0.2290			
$TiSi_2 \\$	$CrSi_2$	T = Ti	0.4426	0.4634			
$CrSi_2$	$TiSi_2 \\$	T = Cr	0.2600	0.2867			
$TiSi_2 \\$	$TiSi_2 \\$	T = Cr	0.0929	0.3440			
$CrSi_2$	$CrSi_2$	T = Ti	0.6648	0.3838			

The origin of this effect can be traced with one more set of calculations: those on  $TiSi_2$  and  $CrSi_2$  in their own structure types but at the cell volumes optimized for the other T element. For  $TiSi_2$ , the smaller atomic radius of Cr compared to Ti ( $r_{Cr}$  = 1.28 Å,  $r_{Ti}$  = 1.47 Å) leads to a 20 % volume reduction. The CP scheme for this compressed geometry yields a QP value of 0.34, which represents a substantial reduction compared to 0.49 for its equilibrium volume. Similarly, the expansion of  $CrSi_2$  to a volume appropriate for T = Ti leads to an increase in the QP metric for the Si site from 0.23 to 0.38. The differences in the quadrupolar character on the Si atoms for  $TiSi_2$  and  $CrSi_2$  can then be largely attributed to their different volumes per formula unit.

The role of cell volume here can be rationalized with a simple picture. The higher packing density of CrSi<sub>2</sub> leads to shorter Si-Si can Cr-Si contacts, which offers a reduced freedom of motion for the Si atoms to shift positions long the T atom channels. This is the very

effect that is foretold by the weaker negative CPs in the Si environments and their lower QP values.

A corollary of this analysis is that expanding the volume of  $CrSi_2$  would open the Si environments, increase their quadrupolar character, and enable similar motions to those that lead to the NCL series. We propose that epitaxial strain on  $CrSi_2$ -type phases induced by their growth on substrates with an appropriate lattice mismatch could lead to superstructure formation and NCL-type structures in a  $CrSi_2$ -type parent lattice. This could also be interesting from the properties point of view:  $CrSi_2$  has been pursued as a thermoelectric material,  $^{69,70,74}$  and superstructures created in this way could offer opportunities for tuning this behavior.

#### 7. FUNCTIONALITY AND CP QUADRUPOLES

In the previous sections, our survey of TE<sub>2</sub> structures connected CP quadrupoles to a range of phenomena, including the emergence of a superstructure through interface insertion, a temperature-driven phase transition, and the opening or closing of helical paths for atomic migration. As our last case study, we consider the CdAs<sub>2</sub> structure type, whose QP character correlates with behavior of a more functional kind: Li intercalation.

The structure comprises a flatted  $\beta$ -Sn-type framework of Cd (similar to that of the Ti atoms of TiSi<sub>2</sub>), with 4-fold helices of As atoms (consistent with a Cd<sup>2+</sup>(As<sup>-</sup>)<sub>2</sub> Zintl bonding type scheme) running along every other square-shaped channel in a checkerboard pattern (Figure 14, left).<sup>75</sup> This inhomogeneous patterning leaves large channels of void spaces between tightly packed channels.

Quadrupoles in the CdAs<sub>2</sub> Type Guide Stuffing Lithions

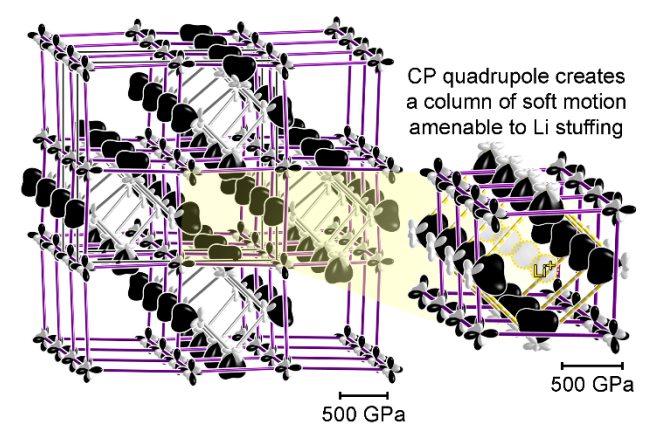


**Figure 14.** The Chemical Pressure scheme of CdAs<sub>2</sub>. Negative pressures on main group atoms point towards void spaces amenable to Li ion stuffing. Inset: negative pressures line the channel thought to host Li ions in  $\text{Lio}_2\text{CdP}_2$ .<sup>76</sup>

These void are, in fact, highlighted by the CP scheme for this structure: the As atoms exhibit large, negative pressures pointing towards the inside of the vacant channels. When the negative lobe on each As atom is combined with the positive pressures it experiences along the As helical motif, a modest QP value of 0.21 arises. The quadrupolar features of the As atoms surround each void space to trace out a helical path of negative pressure within it. The wealth of negative pressure here suggests this space is quite open and could be amenable to denser packing.

The alignment of the negative pressure along this channel suggests an opportunity: one way to alleviate these CPs would be to add

something to the channel, replacing the overlengthened contacts across the empty space with more reasonable contacts to occupants of the channel. In fact, Eckstein et al. discovered that a lithiated variant of CdAs<sub>2</sub>-type CdP<sub>2</sub>, Li<sub>0.2</sub>CdP<sub>2</sub>, can be prepared through direct reaction of the elements.<sup>76</sup> While characterization methods (electron microscopy and solid state NMR) did not precisely locate their positions in the structure,<sup>76</sup> DFT total energy calculations suggested that the preferred sites are within void channels highlighted by CP analysis. The quadrupolar character on the E atoms is also expected to facilitate this process by providing them with a range of easy motion to adjust to the presence of the Li ions.

#### 8. CONCLUSIONS

In this Article, we have explored CP quadrupoles as a potential guide to structural phenomena in intermetallic phases. We first developed a metric to evaluate the quadrupole strengths on atomic sites and applied it to a series of structure types within the TE2 family. A selection of structures and systems with quadrupolar atomic sites were then examined in more detail. Within the Co-Sn system, movement of the Co atoms along soft paths of motion lead to superstructure formation. In the case of CoSb2, the CP distributions on the Sb atoms guide the concerted motion needed to transition to the marcasite polymorph to occur; conversely, the axes of positive pressure on the Sb quadrupoles impedes the motions toward the rutile type, leading to a much higher calculated transition energy. Third, the quadrupoles aligning along helical paths in TiSi2 create a template for soft atomic motions resulting in the NCL structural series, but these motions are inhibited in the related CrSi2 structure, where smaller size of the T atoms leads to a tighter atomic packing that closest up the paths. And finally, Li incorporation in the CdAs2 type was explained in terms of CP quadrupoles whose negative lobes define channels within the structure.

In our survey of TE2 structures, we evaluated CP schemes for 17 structure types, including 44 symmetry-distinct atomic environments. While this is not a large enough sample for deriving statistical conclusions, we note that the distribution of QP values does not sample the full range of 0 to 1, but that sites with values above 0.5 become rare. The most common values are intermediate, in the range of 0.1 to 0.3. The examination of specific systems within this set allows for some calibration of the QP scale. The QP values of 0.39 or 0.27 for the Sb atoms of CoSb<sub>2</sub>, 0.45 for Co in CoSn<sub>2</sub>, and 0.49 for Si in TiSi2 correlate with a low-E phase transition, superstructure formation, and the existence of the chimney ladder series, respectively. Likewise, the smaller value of 0.23 for the Si atoms of CrSi<sub>2</sub> coincides with the absence of structural phenomena that are observed in the related TiSi2 type. Overall, the values of 0.4 and higher seem to represent significant enough quadrupoles for the emergence of interesting effects.

In each of these cases, though, it is not just the QP values that dictate the observed behavior, but the structural context in which they appear. The Si CP quadrupoles in the TiSi2 type each individually offer a soft direction of vibration, but it is their alignment with each other along the T atom channels that allows these vibrational motions to coalesce into helical paths for atomic migration and the NCL series. Likewise, Li incorporation into CdAs2 is supported by the As quadrupoles, despite their relatively small magnitudes of 0.21, because they combine to form large spaces of negative CP. Conversely, the large quadrupoles on the Ge atoms (0.38) of EuGe2

reflect their placement on puckered honeycomb nets and point to the relative softness of the buckling vibrational mode. This would not be expected to support enhanced atomic diffusion through the structure, as the quadrupoles do not form a continuous path, but could enable a phase transition to the  $AlB_2$  type.<sup>77</sup>

Overall, these results point to the CP quadrupole as a descriptor by which intermetallic structures could be screened for potential structural effects or materials behavior related to soft phonon modes. The next step in applying this approach would be expanding the survey of QP character beyond  $TE_2$  systems. The growth of the Intermetallic Reactivity Database (to be presented in a future publication, but already available in preliminary form online) as a repository of CP schemes and other theoretically derived data related to bonding should bring such a comprehensive study within reach. We are looking forward to seeing how the QP concept could then serve as a guide to the experimental investigation of structure-properties relationships.

#### ASSOCIATED CONTENT

This material is available free of charge via the Internet at <a href="http://pubs.acs.org">http://pubs.acs.org</a>.

Further details regarding the QP metric; additional computational details; CP schemes calculated with different assumptions regarding charge transfer in the systems; comparison of the CP features with selected phonon modes for TiSi<sub>2</sub>, CrSi<sub>2</sub>, and CrSi<sub>2</sub>-type TiSi<sub>2</sub>.

#### **AUTHOR INFORMATION**

#### **Corresponding Author**

Daniel C. Fredrickson – Department of Chemistry, University of Wisconsin-Madison, Madison, WI 53706, United States.

Email: danny@chem.wisc.edu

#### Author

Kendall R. Kamp – Department of Chemistry, University of Wisconsin-Madison, Madison, WI 53706, United States.

Present address: Department of Chemistry, Northwestern University, 2145 Sheridan Road, Evanston IL 60208, United States.

#### **ACKNOWLEDGMENT**

We thank Jonathan van Buskirk for his help in depositing the theoretical data obtained in this work in the Intermetallic Reactivity Database. We gratefully acknowledge our financial support from the National Science Foundation (NSF) through grant DMR- 2127349.

#### **REFERENCES**

- (1) Cava, R.; Takagi, H.; Zandbergen, H.; Krajewski, J.; Peck, W.; Siegrist, T.; Batlogg, B.; Van Dover, R.; Felder, R.; Mizuhashi, K. Superconductivity in the quaternary intermetallic compounds  $LnNi_2B_2C$ , *Nature* **1994**, 367, 252-253.
- (2) Gui, X.; Lv, B.; Xie, W. Chemistry in Superconductors, Chem. Rev. 2021, 121, 2966-2991.
- (3) Verchenko, V. Y.; Zubtsovskii, A. O.; Plenkin, D. S.; Bogach, A. V.; Wei, Z.; Tsirlin, A. A.; Dikarev, E. V.; Shevelkov, A. V. Family of Mo<sub>4</sub>Ga<sub>21</sub>-based superconductors, *Chem. Mater.* **2020**, *32*, 6730-6735.
- (4) Buschow, K.; Naastepad, P.; Westendorp, F. Preparation of SmCo<sub>5</sub> permanent magnets, *J. Appl. Phys.* **1969**, *40*, 4029-4032.
- (5) Herbst, J. F.; Croat, J. J.; Yelon, W. B. Structural and magnetic properties of Nd<sub>2</sub>Fe<sub>14</sub>B (invited), *J. Appl. Phys.* **1985**, *57*, 4086-4090.

- (6) Sagawa, M.; Fujimura, S.; Togawa, N.; Yamamoto, H.; Matsuura, Y. New material for permanent magnets on a base of Nd and Fe (invited), *J. Appl. Phys.* **1984**, *55*, 2083-2087.
- (7) DiSalvo, F. J. Thermoelectric cooling and power generation, *Science* **1999**, 285, 703-706.
- (8) Sootsman, J. R.; Chung, D. Y.; Kanatzidis, M. G. New and Old Concepts in Thermoelectric Materials, *Angew. Chem. Int. Ed.* **2009**, *48*, 8616-8639.
- (9) Toberer, E. S.; May, A. F.; Snyder, G. J. Zintl Chemistry for Designing High Efficiency Thermoelectric Materials, *Chem. Mater.* **2010**, *22*, 624-634.
- (10) Snyder, G. J.; Toberer, E. S. Complex thermoelectric materials, In *Materials for Sustainable Energy*; Co-Published with Macmillan Publishers Ltd, UK: 2010, p 101-110.
- (11) Armbrüster, M.; Kovnir, K.; Behrens, M.; Teschner, D.; Grin, Y.; Schlögl, R. Pd–Ga Intermetallic Compounds as Highly Selective Semihydrogenation Catalysts, *J. Am. Chem. Soc.* **2010**, *132*, 14745-14747.
- (12) Lu, Y.; Li, J.; Tada, T.; Toda, Y.; Ueda, S.; Yokoyama, T.; Kitano, M.; Hosono, H. Water Durable Electride Y<sub>5</sub>Si<sub>3</sub>: Electronic Structure and Catalytic Activity for Ammonia Synthesis, *J. Am. Chem. Soc.* **2016**, *138*, 3970-3973.
- (13) Slack, G. A. New materials and performance limits for thermoelectric cooling, In *CRC handbook of thermoelectrics*; CRC Press: 2018, p 407-440.
- (14) Snyder, G. J.; Christensen, M.; Nishibori, E.; Caillat, T.; Iversen, B. B. Disordered zinc in  $Zn_4Sb_3$  with phonon-glass and electron-crystal thermoelectric properties, *Nat. Mater.* **2004**, *3*, 458-463.
- (15) Liang, X.; Chen, C. Ductile inorganic amorphous/crystalline composite Ag<sub>4</sub>TeS with phonon-glass electron-crystal transport behavior and excellent stability of high thermoelectric performance on plastic deformation, *Acta Mater.* **2021**, *218*, 117231.
- (16) Takabatake, T.; Suekuni, K.; Nakayama, T.; Kaneshita, E. Phonon-glass electron-crystal thermoelectric clathrates: Experiments and theory, *Reviews of Modern Physics* **2014**, *86*, 669.
- (17) Gui, X.; Cava, R. J. La $Ir_3Ga_2$ : A Superconductor Based on a Kagome Lattice of Ir, Chem. Mater. **2022**, 34, 2824-2832.
- (18) Jovanovic, M.; Schoop, L. M. Simple Chemical Rules for Predicting Band Structures of Kagome Materials, *J. Am. Chem. Soc.* **2022**, *144*, 10978-10991.
- (19) Gardner, J. S.; Gingras, M. J.; Greedan, J. E. Magnetic pyrochlore oxides, Reviews of Modern Physics 2010, 82, 53.
- (20) McClarty, P. A.; Haque, M.; Sen, A.; Richter, J. Disorder-free localization and many-body quantum scars from magnetic frustration, *Phys. Rev. B* **2020**, *102*, 224303.
- (21) Abramchuk, M.; Ozsoy-Keskinbora, C.; Krizan, J. W.; Metz, K. R.; Bell, D. C.; Tafti, F. Cu<sub>2</sub>IrO<sub>3</sub>: A New Magnetically Frustrated Honeycomb Iridate, *J. Am. Chem. Soc.* **2017**, *139*, 15371-15376.
- (22) Dissanayaka Mudiyanselage, R. S.; Wang, H.; Vilella, O.; Mourigal, M.; Kotliar, G.; Xie, W. LiYbSe<sub>2</sub>: Frustrated Magnetism in the Pyrochlore Lattice, *J. Am. Chem. Soc.* **2022**, *144*, 11933-11937.
- (23) Kamp, K. R.; Fredrickson, D. C. Frustrated Packing in Simple Structures: Chemical Pressure Hindrance to Isolobal Bonds in the TiAl<sub>3</sub> type and ZrAl<sub>2.6</sub>Sn<sub>0.4</sub>, *Inorg. Chem.* **2021**, *60*, 4779-4791.
- (24) Mitchell Warden, H. E.; Fredrickson, D. C. Frustrated and Allowed Structural Transitions: The Theory-Guided Discovery of the Modulated Structure of IrSi, J. Am. Chem. Soc. 2019, 141, 19424-19435.
- (25) Kilduff, B. J.; Fredrickson, D. C. Chemical Pressure-Driven Incommensurability in CaPd<sub>5</sub>: Clues to High-Pressure Chemistry Offered by Complex Intermetallics, *Inorg. Chem.* **2016**, *55*, 6781-6793.
- (26) Engelkemier, J.; Fredrickson, D. C. Chemical Pressure Schemes for the Prediction of Soft Phonon Modes: A Chemist's Guide to the Vibrations of Solid State Materials, *Chem. Mater.* **2016**, 28, 3171-3183.
- (27) Hilleke, K. P.; Fredrickson, R. T.; Vinokur, A. I.; Fredrickson, D. C. Substitution Patterns Understood through Chemical Pressure Analysis: Atom/Dumbbell and Ru/Co Ordering in Derivatives of YCo<sub>5</sub>, Crys. Growth Des. **2017**, *17*, 1610-1619.
- (28) Lu, E.; Fredrickson, D. C. Templating Structural Progessions in Intermetallics: How Chemical Pressure Directs Helix Formation in the Nowotny Chimney Ladders, *Inorg. Chem.* **2019**, *58*, 4063-4066.
- (29) Vinokur, A. I.; Hilleke, K. P.; Fredrickson, D. C. Principles of weakly ordered domains in intermetallics: the cooperative effects of atomic packing and electronics in Fe<sub>2</sub>Al<sub>5</sub>, *Acta Crystallogr. Sect. A: Found. Crystallogr.* **2019**, 75, 297-306

- (30) Gonze, X.; Jollet, F.; Abreu Araujo, F.; Adams, D.; Amadon, B.; Applencourt, T.; Audouze, C.; Beuken, J. M.; Bieder, J.; Bokhanchuk, A.; Bousquet, E.; Bruneval, F.; Caliste, D.; Côté, M.; Dahm, F.; Da Pieve, F.; Delaveau, M.; Di Gennaro, M.; Dorado, B.; Espejo, C.; Geneste, G.; Genovese, L.; Gerossier, A.; Giantomassi, M.; Gillet, Y.; Hamann, D. R.; He, L.; Jomard, G.; Laflamme Janssen, J.; Le Roux, S.; Levitt, A.; Lherbier, A.; Liu, F.; Lukačević, I.; Martin, A.; Martins, C.; Oliveira, M. J. T.; Poncé, S.; Pouillon, Y.; Rangel, T.; Rignanese, G. M.; Romero, A. H.; Rousseau, B.; Rubel, O.; Shukri, A. A.; Stankovski, M.; Torrent, M.; Van Setten, M. J.; Van Troeye, B.; Verstraete, M. J.; Waroquiers, D.; Wiktor, J.; Xu, B.; Zhou, A.; Zwanziger, J. W. Recent developments in the ABINIT software package, Comput. Phys. Comm. 2016, 205, 106-131.
- (31) Gonze, X.; Beuken, J. M.; Caracas, R.; Detraux, F.; Fuchs, M.; Rignanese, G. M.; Sindic, L.; Verstraete, M.; Zerah, G.; Jollet, F.; Torrent, M.; Roy, A.; Mikami, M.; Ghosez, P.; Raty, J. Y.; Allan, D. C. First-principles computation of material properties: the ABINIT software project, *Comput. Mater. Sci.* **2002**, 25, 478-492. (32) Gonze, X. A brief introduction to the ABINIT software package, *Z. Kristallogr.* **2005**, 220, 558-562.
- (33) Gonze, X.; Amadon, B.; Anglade, P.-M.; Beuken, J.-M.; Bottin, F.; Boulanger, P.; Bruneval, F.; Caliste, D.; Caracas, R.; Côté, M. ABINIT: First-principles approach to material and nanosystem properties, *Comput. Phys. Comm.* **2009**, *180*, 2582-2615.
- (34) Goedecker, S.; Teter, M.; Hutter, J. Separable dual-space Gaussian pseudopotentials, *Phys. Rev. B* **1996**, *54*, 1703.
- (35) Hartwigsen, C.; Goedecker, S.; Hutter, J. Relativistic separable dual-space Gaussian pseudopotentials from H to Rn, *Phys. Rev. B* **1998**, *58*, 3641.
- (36) Hilleke, K. P.; Fredrickson, D. C. Discerning Chemical Pressure amidst Weak Potentials: Vibrational Modes and Dumbbell/Atom Substitution in Intermetallic Aluminides, *J. Phys. Chem. A* **2018**, *122*, 8412-8426.
- (37) Berns, V. M.; Engelkemier, J.; Guo, Y.; Kilduff, B. J.; Fredrickson, D. C. Progress in Visualizing Atomic Size Effects with DFT-Chemical Pressure Analysis: From Isolated Atoms to Trends in  $AB_5$  Intermetallics, *J. Chem.* **2014**, *10*, 3380-3392.
- (38) Lu, E.; Van Buskirk, J. S.; Cheng, J.; Fredrickson, D. C. Tutorial on Chemical Pressure Analysis: How Atomic Packing Drives Laves/Zintl Intergrowth in  $K_3Au_5Tl$ , Crystals **2021**, 11, 906.
- (39) Sanville, E.; Kenny, S. D.; Smith, R.; Henkelman, G. Improved grid-based algorithm for Bader charge allocation, *J. Comput. Chem.* **2007**, *28*, 899-908.
- (40) Tang, W.; Sanville, E.; Henkelman, G. A grid-based Bader analysis algorithm without lattice bias, *J. Phys.: Condens. Matter* **2009**, *21*, 084204.
- (41) Henkelman, G.; Arnaldsson, A.; Jónsson, H. A fast and robust algorithm for Bader decomposition of charge density, *Comput. Mater. Sci.* **2006**, *36*, 354-360.
- (42) Bader, R. F. W. Atoms in molecules, Acc. Chem. Res. 1985, 18, 9-15.
- (43) Oliveira, M. J.; Nogueira, F. Generating relativistic pseudo-potentials with explicit incorporation of semi-core states using APE, the Atomic Pseudo-potentials Engine, *Comput. Phys. Commun.* **2008**, *178*, 524-534.
- (44) Kresse, G.; Joubert, D. From ultrasoft pseudopotentials to the projector augmented-wave method, *Phys. Rev. B* **1999**, *59*, 1758-1775.
- (45) Kresse, G.; Furthmüller, J. Efficient iterative schemes for ab initio totalenergy calculations using a plane-wave basis set, *Phys. Rev. B* **1996**, *54*, 11169-11186.
- (46) Kresse, G.; Hafner, J. Ab initio molecular-dynamics simulation of the liquid-metal–amorphous-semiconductor transition in germanium, *Phys. Rev. B* **1994**, 49, 14251.
- (47) Kresse, G.; Hafner, J. Ab initio molecular dynamics for liquid metals, *Phys. Rev. B* **1993**, 47, 558.
- (48) Perdew, J. P.; Chevary, J. A.; Vosko, S. H.; Jackson, K. A.; Pederson, M. R.; Singh, D. J.; Fiolhais, C. Atoms, molecules, solids, and surfaces: Applications of the generalized gradient approximation for exchange and correlation, *Phys. Rev. B* **1992**, *46*, 6671-6687.
- (49) Perdew, J. P.; Chevary, J.; Vosko, S.; Jackson, K. A.; Pederson, M. R.; Singh, D.; Fiolhais, C. Erratum: Atoms, molecules, solids, and surfaces: Applications of the generalized gradient approximation for exchange and correlation, *Phys. Rev. B* **1993**, *48*, 4978.
- (50) Blöchl, P. E. Projector augmented-wave method, *Phys. Rev. B* **1994**, *S0*, 17953-17979.
- (51) Gonze, X. First-principles responses of solids to atomic displacements and homogeneous electric fields: Implementation of a conjugate-gradient algorithm, *Phys. Rev. B* **1997**, *55*, 10337-10354.

- (52) Yannello, V. J.; Fredrickson, D. C. Generality of the 18-*n* Rule: Intermetallic Structural Chemistry Explained through Isolobal Analogies to Transition Metal Complexes, *Inorg. Chem.* **2015**, *54*, 11385-11398.
- (53) Miyazaki, K.; Yannello, V. J.; Fredrickson, D. C. Electron-counting in intermetallics made easy: the 18-*n* rule and isolobal bonds across the Os-Al system, *Z. Kristallogr. Cryst, Mater.* **2017**, 232, 487-496.
- (54) Bergerhoff, G.; Hundt, R.; Sievers, R.; Brown, I. The Inorganic Crystal Structure Database, J. Chem. Inf. Comput. Sci. 1983, 23, 66-69.
- (55) Grin, Y.; Wagner, F. R.; Armbrüster, M.; Kohout, M.; Leithe-Jasper, A.; Schwarz, U.; Wedig, U.; Georg von Schnering, H. CuAl<sub>2</sub> revisited: Composition, crystal structure, chemical bonding, compressibility and Raman spectroscopy, *J. Solid State Chem.* **2006**, *179*, 1707-1719.
- (56) Armbrüster, M.; Schnelle, W.; Cardoso-Gil, R.; Grin, Y. Chemical Bonding in Compounds of the CuAl<sub>2</sub> Family: MnSn<sub>2</sub>, FeSn<sub>2</sub> and CoSn<sub>2</sub>, *Chem Eur. J.* **2010**, *16*, 10357-10365.
- (57) Lang, A.; Jeitschko, W. Two new phases in the system cobalt-tin: the crystal structures of  $\alpha$ -and  $\beta$ -CoSn<sub>3</sub>, Z Metallkd **1996**, 87, 759-764.
- (58) Greenwood, N. N.; Earnshaw, A. In Chemistry of the Elements (Second Edition); Butterworth-Heinemann: Oxford, 1997, p 216-267.
- (59) Kjekshus, A. Properties of Binary Compounds with the CoSb<sub>2</sub>-type Crystal Structure, *Acta Chem. Scand. Ser. A.* **1971**, *25*, 411-422.
- (60) Zhdanov, G.; Kuz'min, R. Structure of Compounds in the MSb<sub>2</sub> Group: CoSb<sub>2</sub>, RhSb<sub>2</sub>, IrSb<sub>2</sub>, and α-RhBi<sub>2</sub>, Kristallografiya **1961**, *6*, 872-881.
- (61) Siegrist, T.; Hulliger, F. High-temperature behavior of CoAs<sub>2</sub> and CoSb<sub>2</sub>, *J. Solid State Chem.* **1986**, *63*, 23-30.
- (62) Okamoto, H. Co-Sb (Cobalt-Antimony), J. Phase Equilibria Diffus. 2005, 26, 198.
- (63) Baur, W. H.; Khan, A. A. Rutile-type compounds. IV. SiO<sub>2</sub>, GeO<sub>2</sub> and a comparison with other rutile-type structures, *Acta Crystallogr. Sect. B* **1971**, 27, 2133-2139.
- (64) Wolf, W.; Bihlmayer, G.; Blügel, S. Electronic structure of the Nowotny chimney-ladder silicide Ru<sub>2</sub>Si<sub>3</sub>, *Phys. Rev. B* **1997**, 55, 6918-6926.
- (65) Harada, Y.; Morinaga, M.; Saso, D.; Takata, M.; Sakata, M. Refinement in crystal structure of MoSi<sub>2</sub>, *Intermetallics* **1998**, *6*, 523-527.
- (66) Pearson, W. B. The Crystal Chemistry and Physics of Metals and Alloys; Wiley-Interscience: New York, 1972.
- (67) Jeitschko, W.; Holleck, H.; Nowotny, H.; Benesovsky, F. Die Verbindungen RuGa und RuGa<sub>2</sub>, *Monatsh. Chem.* **1963**, *94*, 838-840.
- (68) Fredrickson, D. C.; Lee, S.; Hoffmann, R.; Lin, J. The Nowotny Chimney Ladder Phases: Following the pseudo Clue toward an Explanation of the 14 Electron Rule, *Inorg. Chem.* **2004**, *43*, 6151-6158.
- (69) Opahle, I.; Parma, A.; McEniry, E. J.; Drautz, R.; Madsen, G. K. H. Highthroughput study of the structural stability and thermoelectric properties of transition metal silicides, *New J. Phys.* **2013**, *15*, 105010.
- (70) Dasgupta, T.; Etourneau, J.; Chevalier, B.; Matar, S. F.; Umarji, A. M. Structural, thermal, and electrical properties of CrSi<sub>2</sub>, *J. Appl. Phys.* **2008**, *103*, 113516.
- (71) Schwomma, O.; Nowotny, H.; Wittmann, A. Untersuchungen im System: Ru–Sn, *Monatsh. Chem.* **1964**, *95*, 1538-1543.
- (72) Völlenkle, H.; Wittmann, A.; Nowotny, H. Die Kristallstrukturen von  $Rh_{10}Ga_{17}$  und  $Ir_3Ga_5$ , Monatsh. Chem. **1967**, 98, 176-183.
- (73) Panday, P. K.; Singh, G. S. P.; Schubert, K. Kristallstruktur von Ir<sub>4</sub>Ge<sub>5</sub>, Z. Kristallogr. Cryst, Mater. **1967**, 125, 274-285.
- (74) Timm, M.; Oliviero, E.; Sun, W.; Gomes, S.; Hamaoui, G.; Fichtner, P.; Frety, N. Ion implantation effects on the microstructure, electrical resistivity and thermal conductivity of amorphous CrSi<sub>2</sub> thin films, *J. Mater. Sci.* **2022**, 1-12.
- (75) Cervinka, L.; Hruby, A. The crystal structure of CdAs<sub>2</sub>, Acta Crystallogr. Sect. B 1970, 26, 457-458.
- (76) Eckstein, N.; Krüger, I.; Bachhuber, F.; Weihrich, R.; Barquera-Lozada, J. E.; van Wüllen, L.; Nilges, T. Low-activated Li-ion mobility and metal to semiconductor transition in CdP<sub>2</sub>@Li phases, *J. Mater. Chem.* **2015**, *3*, 6484-6491.
- (77) Imai, M.; Kikegawa, T. Phase Transitions of Alkaline-Earth-Metal Disilicides MAESi<sub>2</sub> (MAE = Ca, Sr, and Ba) at High Pressures and High Temperatures, *Chem. Mater.* **2003**, *15*, 2543-2551.

### For Table of Contents Use Only

